# Bioinspired nanovalves with selective permeability and pH sensitivity

Z. Zheng[a,b], X. Huang[c], M. Schenderlein[a], H. Moehwald[a], G.-K. Xu[d] and D. G. Shchukin[b]

Biological systems with controlled permeability and release functionality, which are among the successful examples of living beings to survive in evolution, have attracted intensive investigation and mimicked due to their broad spectrum of applications. We present in this work for the first time an example of nuclear pore complexes (NPCs)-inspired controlled release system that exhibits on-demand release of angstrom-sized molecules. We do so in a cost-effective way by stabilizing porous cobalt basic carbonates as nanovalves and realizing pH-sensitive release of entrapped subnano cargo. The proof-of-concept work also consists of establishment of two mathematic models to explain the selective permeability of the nanovalves. Finally, gram-sized quantities or more of the bio-inspired controlled release system can be synthesized through a scaling-up strategy, which opens up opportunities for controlled release of functional molecules in wider practical applications.

## 1. Introduction

The bio-mimic/inspired release systems, for example, the cell mimic polyersomes[1], have been tailored to be sensitive to a wide range of stimuli[2] (e.g. pH, light, temperature, redox, electrostatic force, magnetic field and ultrasound). So far, however, such biomimic controlled release systems performed effectively for cargo molecules with at least one dimension larger than 1 nm, such as drugs (≥ 5 nm)[3-6], enzymes (≥ 10 nm), proteins (≥ 50 nm)[7,8] and cells (~10-30 μm)[9,10]. At the other extreme, the active channels that only allow the transport of metal ions (always below 1 Å) across double-layer liposome membranes are recently focused on, resulting in man-made organic helical pores[11-13] and hybrid ion pumps[14,15]. Noteworthy is that many other functional molecules with angstrom dimensions have been found to not only play an equally vital role as their larger and smaller counterparts in physiology[16] but to be more applicable and durable in other applications, such as self-healing materials[17,18]. However, we found the existing mechanisms for controlled release mainly depended on sealing/unsealing the pores[19,20] or switching the charge of orifices, which would, in many cases, fail in valving the low molecular weight compounds[21].

Herein, we present, to the best of knowledge, the first example of nuclear pore complexes (NPCs)-inspired controlled release system that exhibits on-demand release of angstrom-sized molecules. NPCs as an effective valve system are located at the nuclear envelope and can control the nucleo-cytoplasmic exchange[22,23]. Equipped with a three dimensional (3D) sieve-like barrier, NPCs are freely permeable for small molecules, and set passive exclusion to cargoes larger than ~30 to 40 kD[24] but accelerate the transportation of even larger ones that can form reversible complex with nuclear transport receptors[25,26]. Such a reversible complexation for selective permeability was found in 1990s, but there was hardly any derivative design for controlled release device yet. It is mainly due to the difficulty in realizing it in an inanimate system in a cost-effective way and evaluating the permeability of the valve structure except in hydrogel-like state[26]. To address these issues and effectively control the release of the subnano-sized functional molecules, we are inspired by the NPCs, but with a seemingly opposite demand: the expected nanovalves should selectively suppress the flux of small compounds that can interact reversibly with valve structure and, meanwhile, are size-dependently permeable for other inert cargoes.

We examine the easily handled and cost-effective 3D porous transition metal precipitates, for example, nano-sized cobalt basic carbonates (Co-Carbonate), to understand how the reversible complexation works for the selective permeability. The porous structure of nanovalves and the complex bonds between metal ions and functional molecules allow us to formulate mathematical model for the semi-quantitative permeability evaluation of the nanovalves for the diffusion of molecules that interact with $Co^{2+}$ centers with different stability constants. Finally, we show a facile method to fabricate a NPCs-inspired controlled release system that can be easily scaled up to the application quantities. We believe that this proof-of-concept work and scaling-up strategy have great potential to enrich the selection of controlled release method and enable various novel designs in the applications outside biomedicine or drug delivery, for example the feedback self-healing painting, environmental evaluation, industrial catalysis and modern fertilizer technology.

## 2. Experimental section

**2.1 Ethylenediamine triacetic acid functionalized silica MCM-41 nanocontainers.** The bared mesoporous silica solid (2 g) was fabricated[27] and suspended in 500 mL of dry toluene, to which 0.14 mL of (trimethoxysilylpropyl)-ethylenediamine triacetic acid trisodium salt aqueous solution (45% in water) was added. The mixture was continuously stirred at 120 °C for 20 h, resulting in MCM-41 functionalized with ethylenediamine triacetic acid.

**2.2 Synthetic procedure and scaling up strategy.** A sprayer was used for forming nanovalves on the loaded containers in a large amount. Typically, 0.1 M $Co(NO_3)_2$ solution (2~3 mL) was sprayed on 2 g of loaded containers followed by removing salt excess. The same amount of 0.2 M $Na_2CO_3$ solution was then sprayed. The resulting product was sealed for 3-days aging and then introduced in coating matrix for self-healing corrosion protection.

**2.3 Small-angle X-ray scattering (SAXS) measurements.** The transition metal precipitates injected in capillary (1.5 mm in diameter, Borokapillaren, GLAS) were investigated for information about porous structure. SAXS profiles were recorded under vacuum on a Nanostar instrument (Bruker AXS) using Cu-K α radiation with a wavelength of λ= 0.154 nm. A single photon counting area detector (HiStar, Bruker AXS) was used at a sample-detector distance of 25.2 cm and a range of scattering vector q from 0.035 to 0.7 $nm^{-1}$ was covered. The capillaries stood vertically during aging for 1, 3 and 10 days. During measurement they were horizontal.

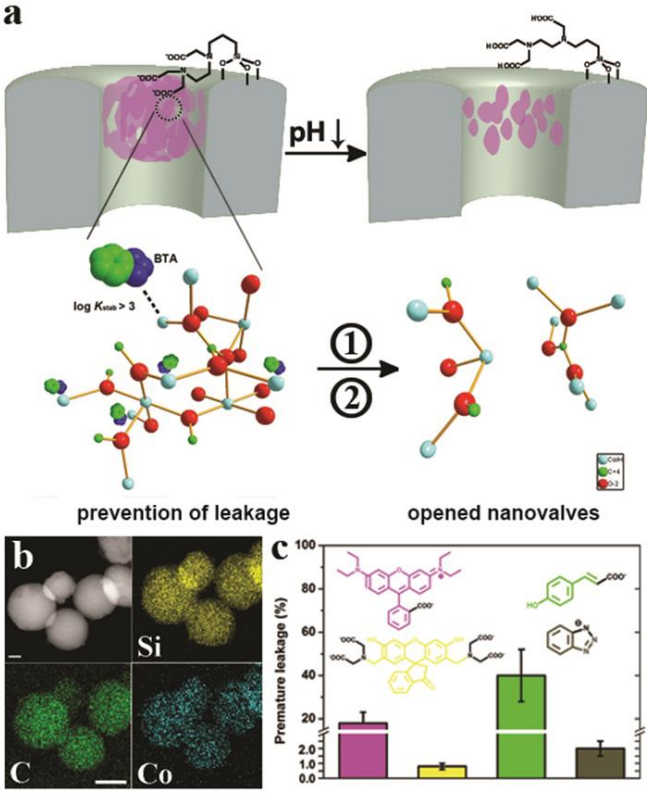


Fig. 1. (a) Schematic representation of components forming the nanovalve system, mechanism of selective permeability and pH response of it. Lowering the pH value will 1) dissociate the $Co^{2+}$-cargo complex bonding and 2) destroy the structure of nanovalves gradually. The two lower cartoons are modified from crystal structure of $CoCO_3$ to highlight the complexation between cargo and nanovalves, as well as acid induced partial and gradual dissolution of valve structure, and dissociation of $Co^{2+}$-cargo complex bonding. (b) HAADF-STEM and elemental mapping images of loaded MCM-41 nanoparticle with nanovalves at its surface. Silicon, carbon and cobalt element mapping are presented. Scale bar: HAADF-STEM 50 nm, elemental mapping 100 nm. (c) Premature leakage of Rhodamine B (purple), calcein (yellow), p-coumaric acid (green) and BTA (grey) from containers sealed by Co-Carbonate nanovalves.

**2.4 Selective adsorption measurement.** To test permeability of the precipitates, a special quartz cuvette (10 mm width) was designed, as shown in Scheme S1†. The precipitates or water were confined in a space formed by upper membrane, lower membrane (MWCO 12 000 - 14 000 for both) and inner wall of the tube inserted into cuvette at 1 cm depth. On the upper membrane, 1 mL of starting solution was placed. The solution in cuvette was stirred moderately by a 5-mm stirring bar to balance the concentration of interesting molecules. The solution was monitored using fluorescence spectroscopy (FluoroMax-4, HORIBA Jobin Yvon). A laser probe beam was directed into the solution at 2 cm above the bottom and around 1 cm below the top of the cuvette.

**2.5 pH sensitive release.** UV-vis spectroscopy (8453 UV-visible spectrophotometer, Agilent technologies) were applied to determine the release profile of BTA. The 1 mg powder was placed in the bottom of a small bag which is made of a screen mesh membrane with mesh at around 1 μm. Then, buffer solution (at pH ≈ 7, 4 mL) was added to the cuvette till the bottom of the bag was immersed into water. The UV detector focuses into the solution at 2 cm above the bottom and around 1 cm below the top of the cuvette. The absorbance of BTA at 275 nm was plotted as a function of time in order to generate a release profile. The final concentration of BTA was determined by UV spectroscopy. Stimulated release of BTA from the containers was accomplished by changing the neutral solution with the one with lower pH value.

**2.6 Self-healing anticorrosion analysis.** Scanning Vibration Electrode Technique (SVET) measurements and Electrochemical Impedance Spectroscopy (EIS) experiments have been described in our previous work[28].

## 3. Results and discussion

**3.1 Characterization of NPCs-inspired controlled release system.** We examined the easily handled, cost-effective and nano-sized cobalt basic carbonates (Co-Carbonate) for nanovalves. Fig. 1a shows that the NPCs-inspired controlled release system consists of a 3D porous Co-Carbonate nanovalve which is stabilized at an orifice of the ethylenediamine triacetate functionalized silica nanocontainer (Figs. S1-2†). The nanovalve, formed by rapid reaction between $Co^{2+}$ and $CO_3^{2-}$/$OH^-$[29], is insoluble in neutral environment but can respond to pH lowering by dissolution of valve structure (Route 1 in Fig. 1a). The cargo molecules that complex strongly with $Co^{2+}$, e.g. *1H*-benzotriazole (BTA, anticorrosion agent, more information in ESI) that complexes with cobalt ions with stability constant (log $K_{stab}$) > 3[30], are preferably detained in the pores of nanocontainers, resulting in the prevention of premature leakage. The reversible bonds can dissociate in response to a pH lowering due to the protonation of electron donating agents [31,32], which enables the nanovalves to release the entrapped cargo as a feedback to the external trigger (Route 2 in Fig. 1a).
Fig. 1b shows a high angle annular dark-field scanning transmission electron microscopy (HAADF-STEM) image and elemental mapping of loaded MCM-41 nanoparticles with nanovalves at their surfaces. Co-Carbonate nanovalves are undetectable either in STEM or TEM (Fig. S2†) because of their amorphous phase[33] (Fig. S4†, XRD result in ESI) and unstable structure under high energy beam. But the Co mapping confirms the distribution of the cobalt signal over the surface of the particles. Besides, the high signal contrast of carbon distribution between particle surface and carbon grid underneath confirms the presence of stabilizing agents and Co-Carbonates nanovalves. About 1.7±0.3 wt% of Co content can be confirmed by energy-dispersive X-ray spectroscopy (EDX). The stabilizing effect offered by ethylenediamine triacetate has been demonstrated in detail in our previous work[34], we focus here on the selective permeability of different cargo molecules through the Co-Carbonate nanovalves.

**3.2 Premature leakage study**. To examine the NPCs-inspired controlled release system, we test two pairs of cargoes with comparable sizes but different functional ending groups, namely rhodamine B (15 Å) and *p*-coumaric acid (4.5 Å) serving as free diffusing molecules, and calcein (16.5 Å) and BTA (4 Å) as representatives of selectively detained cargoes. The loading amounts of the four cargoes (by TGA) are 4.2, 13.5, 3.6 and 24.7 wt%, respectively. Fig. 1c reveals that the nanovalve system leads to a size-dependent leakage of rhodamine B (18% of the loading) and *p*-coumaric acid (40%). For calcein and BTA, which have comparable molecular size with the former ones, but the leakage is substantially suppressed: 0.8% for calcein and 2% for BTA. The nanovalves are believed to have stronger affinity for the latter two cargoes because the stability constants for the complex of $Co^{2+}$ with triazole derivatives and iminodiacetic acids[35] are generally at the range of 3~4 and 7~8, respectively, while the metal-carboxylate complexes are always below 1[36].

**3.3 Structural analysis of Co-Carbonate nanovalves.** A small angle x-ray scattering (SAXS) study helps to explain the performance in premature leakage. Fig. 2a reveals two successive power-law regimes at the Porod region[37] of **Co-Carbonate** gelatinous precipitates (curve III) after one-day aging, with the slopes of -2.2 and -2.9. The slopes increase to -2.3 and -3.3 (Fig. 2b) at the end of aging, indicating a precipitate with a mass fractal regime (d*f* = 2.3) and a surface fractal regime (d*s* = 2.7). The crossover occurs at $K = 0.12$ Å$^{-1}$, corresponding to a thickness of backbone, $K^{-1} = 8.3$ Å. The most reasonable structure of the **Co-Carbonate** precipitates can be deduced considering the conclusion reported by Schaefer and Keefer[38], which is a 3D ag**g**regate with rough pores and fractal backbones. In addition, measuring the Guinier radius from the initial curvature of the scattering curves[39] (Fig. S5†, Guinier regime analysis) also allows us to determine the radius of gyration of **Co-Carbonate** precipitates at around 22 Å which is in close to the pore diameter of functionalized silica orifice (26 Å).

We also referred to Ni-Carbonate, Co-Phosphate and Ni-Phosphate (nickel basic carbonates, cobalt phosphates and nickel phosphates in Table S1†, curve I, II and IV) precipitates which remain their single mass fractal states without evidence of conversion to the self-supporting porous structure[40], as observed in Fig. 2b. Fe-Phosphate and Zn-Phosphate samples (iron phosphate and zinc phosphate, curve V, VI) are surface fractals with their slope values unchanged above 3 during the aging process, indicating that they are just stabilized in a colloidal state. The measured zeta-average diameters of them are 195.5 ± 1.7 and 215.3 ± 1.0 nm. The test for premature leakage from containers sealed with these structures reveals no retard for free diffusing molecules and uncontrollable release for selectively detained cargoes. We ascribe it to the lack of 3D porous structure and the mismatch in size between valve and orifice of containers. (Fig. S3†) Furthermore, the largest surface area ($S_{BET}$ = 75.28 m$^2$/g) but modest surface charge (21.6 mV) of the Co-Carbonate sample confirm its 3D self-supporting porous structure (Table S2†).

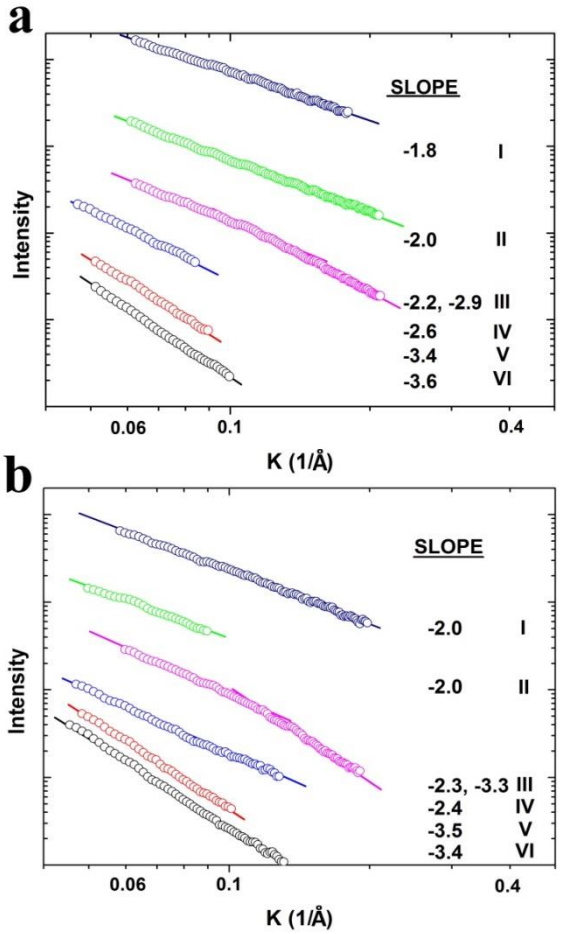


Fig. 2. Porod plots and corresponding slopes of Ni-Carbonate (I, Navy), Co-Phosphate (II, Green), Co-Carbonate (III, Magenta), Ni-Phosphate (IV, Blue), Fe-Phosphate (V, Red) and Zn-Phosphate (VI, Black) after 1-day (a) and 3-days (b) aging at room temperature. In the Porod region the scattered intensity decays as a power law: $I(K) \sim K^{-D}$. Thus the fractal dimension is $D = -2df + ds$ where D is obtained from the value of the slope at the Porod region, df is the mass fractal dimension ($0 \leq df \leq 3$) and ds is the surface fractal dimension ($2 \leq ds \leq 3$).

**3.4 Models for evaluating the permeability of NPCs-inspired nanovalves.** The question comes after the confirmation of 3D porous nanovalves: how the nanovalves act towards different cargo molecules and how to quantitatively evaluate the effect? To avoid the interference from container's interior surface or chelating agents, a homemade setup (Scheme S1†) was built for real-time fluorescence measurement. We began by considering model (1), as shown in Fig. 3a left, where the transition metal precipitates set only size-selective barrier for the molecular diffusion. The solute concentration in cuvette as a function of time can be written as:

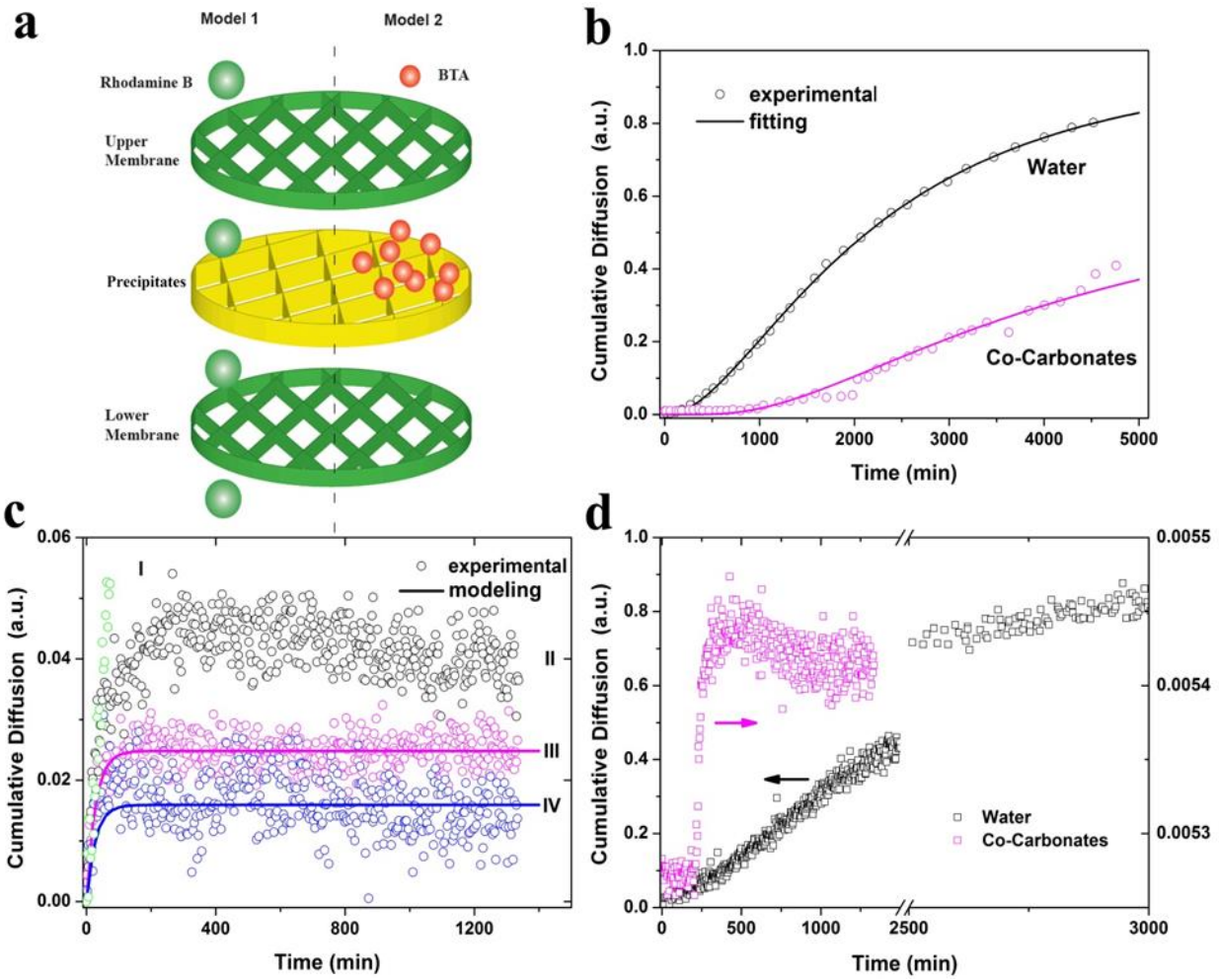


Fig. 3. (a) Scheme depicts the selective permeability for rhodamine B as free diffusing molecules in model (1) and BTA as selectively detained molecules in model (2). (b) The concentration of rhodamine B in cuvette (circle) as a function of time. The mathematic model (solid curves) is consistent with the trend of experimental data when water and Co-Carbonate nanovalves are located between two membranes. (c) The concentration of BTA in cuvette (circle) as a function of time as 1 mM (I), 100 mM (III) and 1 M (IV) of Co-Carbonate precipitates are utilized and concentration of starting solution is 10 mg/L. Data III and IV are fitted with equation (2). II represents the case when saturated BTA solution diffused through system with 100 mM Co-Carbonate precipitates. (d) Calcein is selectively absorbed by Co-Carbonate precipitates. The initial lag phase is attributed to the reluctance of calcein diffusion through semi-permeable upper and lower membranes.

$$c(t) = c_{t\to\infty}(1-e^{-At})\cdot erfc\left(\frac{F}{\sqrt{t}}\right)\cdot(1-e^{-Bt}) \qquad (1)$$

where $c_{t\to\infty}$ is the final equilibrium concentration, the terms $(1-e^{-At})$ and $(1-e^{-Bt})$ represent the fraction of solutes diffused through the upper and lower membranes[41], respectively; $erfc(F/\sqrt{t})$ corresponds a modified complementary error function depicting a simple case of diffusion with time $t$ in one dimension. The values of parameter $F$ belonging to different types of precipitates (Table 1) are semi-quantitatively evaluated by modelling the equation (1). The initial concentration of all solutions above upper membrane is 100 mg/L which falls in the linear fluorescence intensity-concentration range. Figs. 3b and S6† shows the fitting outcome superposes onto the measured (normalized with equilibrium concentration) rhodamine B concentration, supporting the rationale for model (1). Provided the weak stability of $Co^{2+}$-carboxylate complexes[36], the 3D porous Co-Carbonate nanovalves serve only as a "chromatographic column filler" to retard the diffusion of rhodamine B, although they exhibit a lag phase longer than 1000 min, a quite gentle burst phase[40] and a high value of $F$ (40.84 $min^{1/2}$). Equation (1) can still fit the experimental data of *p*-coumaric acid, yielding lower $F$ values (Table 1), which can be attributed to the weaker steric hindrance of membranes and precipitates to the smaller size of solutes. Model (1) matches the diffusion profile of molecules that easily detach from the divalent metal ion centers, but cannot reliably describe the ones which are detained strongly, essential for selective entrapment offered by nanovalves. Thus we developed model (2), illustrated in Fig. 3a right, where BTA molecules complex strongly with $Co^{2+}$ centers in porous structure. Again, the concentration signal in cuvette as a function of time can be expressed as:

$$c(t) = c_{t\to\infty}(1-e^{-At})\cdot\left(\frac{1}{1+c_{t\to\infty}(1-e^{-At})L}\right)\cdot(1-e^{-Bt}) \qquad (2)$$

where $L$ corresponds to the Langmuir adsorption constant. Equation (2), which replaces the simple diffusion term of equation (1) with a residue term of Langmuir adsorption[42], accounts for the capacity of precipitates to capture the solute molecules. Accordingly, we modelled using equation (2) to semi-quantitatively evaluate selective adsorption provided by nanovalves. Co-Carbonate nanovalves in 100 mM obstruct the diffusion of appropriately 97% of BTA (Fig. 3c,

curve III), when the starting concentration is 10 mg/ml. The value of *L* obtained from the fit is 2203.35 ml/mg, which exceeds other precipitates except Ni-Carbonate. The nanovalves can still detain more than 95% of BTA molecules from saturated initial solution (~20 mg/ml, curve II). Further changing the concentration of nanovalves (curve I and IV) illustrates that 1 mM leads to only 60% of the BTA detained (Figs. 2c and S7†), but 1 M can only improve 1% more BTA blockage than 100 mM, implying that 100 mM may be the "saturation limit" for maintaining effective adsorption. Other molecules that form stable complex with $Co^{2+}$ can also be selectively detained by **Co-Carbonate** nanovalves (Fig. 3d), with for example only 0.5% of the calcein molecules detected in cuvette. 80% of them, on the contrary, complete Model (1) diffusion when the nanovalves are replaced by water.

Table 1. Data derived from theoretical modelling.

| | $F^a$ ($min^{1/2}$) | $F^b$ ($min^{1/2}$) | $L^c$ (mL/mg) |
|---|---|---|---|
| water | 4.63 | 2.75 | |
| Ni-Carbonate | 57.89 | 43.28 | 8719.33 |
| Ni-Phosphate | 26.29 | 18.10 | 857.84 |
| Co-Carbonate | 40.84 | 30.67 | 2203.35 |
| Co-Phosphate | 13.87 | 9.39 | 528.27 |
| Fe-Phosphate | 24.01 | 16.47 | 600.02 |
| Zn-Phosphate | 21.91 | 12.24 | 583.23 |

[a] Case of Rhodamine B, [b] case of p-coumaric acid, [c] case of BTA. F represents the ability of precipitates to limit the free diffusion of the solute. L is Langmuir adsorption constant depicting the capacity of surface to absorb the solute.

**3.5 pH response of NPCs-inspired controlled release system.** The instinct pH sensitivity of the composite structure of Co-Carbonate nanovalves is examined in a titration experiment where a broad equivalence point recognition criteria (ERC) peak is observed at pH range of 6 to 2 (Fig. S8†), indicating the nanovalves can be gradually dissolved in response to pH lowering. Fig. 4a shows a flat baseline at neutral environment for the capped sample, implying a negligible premature leakage from containers covered by **Co-Carbonate** nanovalves. At pH=5, more than 80% of the loaded BTA is released in almost 12 hours. Further lowering the pH value to 2 accelerates the gush and more BTA (above 90%) comes out due to protonation of chelating agents[43]. Thus, we believe the NPCs-inspired controlled release system can rapidly and rationally respond to bulky and microenvironmental pH lowering which is usually resulted from hydrolysis of trivalent ions ($Fe^{3+}$ and $Al^{3+}$) from defects in steel or aluminum alloy substrates[44].

**3.6 Scale-up for self-healing anticorrosive application.** As a final step towards achieving our goal of scaling up the NPCs-inspired controlled release system for self-healing applications, we sprayed in sequence the solution of $Co(NO_3)_2$ and $Na_2CO_3$ directly onto the loaded functionalized-MCM-41 powder (up to 5 g), and then integrated the wet grey purple powder (Fig. 4b) with the water-borne epoxy coating matrix. Single layer coatings were applied on Al alloy AA2024-T3 plates for 50 μm wet coating thickness[45].

Scanning vibrating electrode technique (SVET) is employed to detect the current flow caused by corrosion above the artificial pitting corrosion sites where the local pH lowering has been experimentally proved[46]. Before measurement, we put the scratched samples in a flowing artificial seawater environment to remove free inhibitors. Fig. 4c depicts that the corrosion propagation of the sample covered by hybrid coating incorporating 5 wt% NPCs-inspired controlled release system (thus 1 wt% entrapped BTA) is obviously suppressed with the anodic current density lower than 2 $\mu A/cm^2$. A dense film formed by released BTA and copper ions in Al alloy substrate cover the metal surface, resulting in corrosion termination[47]. On the contrary, the increasing values can be seen with the sample covered by blank epoxy and commercial dummy coating which

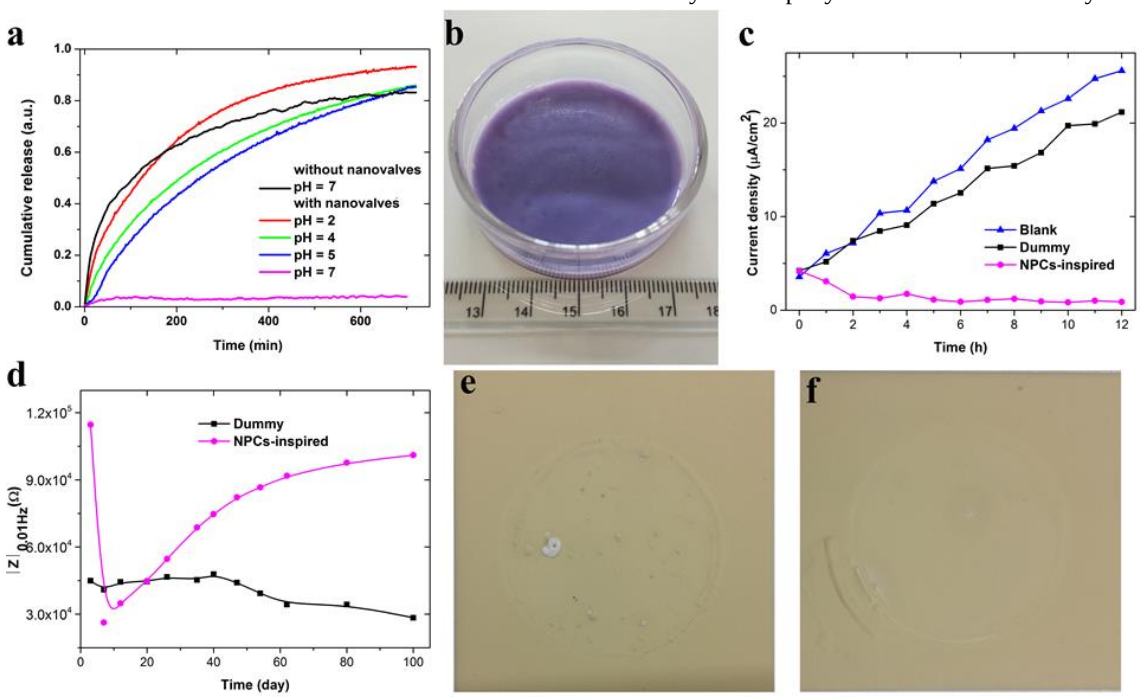


Fig. 4. (a) pH sensitive release profile of BTA from the loaded nanocontainers with Co-Carbonate nanovalves. (b) NPCs-inspired controlled release system fabricated via scaling-up strategy. (c) SVET measurement: the anodic corrosion propagation of the samples covered by blank epoxy coating, commercial dummy coating and the hybrid coating containing 5 wt% NPCs-inspired controlled release system, in the time range of 12h. (d) Impedance |Z| measured at 0.01 Hz in 100 days range for dummy coating and hybrid coating containing NPCs-inspired controlled release system. (e, f) are photographs of the samples coated with dummy coating and hybrid coating after 100 days immersion in 1 M NaCl solution.

contains 5 wt% free BTA. It is obvious that the effective prevention of the premature leakage from nanocontainers maintains the potential of anticorrosion and enables the rapid self-healing effect to the corrosion site.

The hybrid coating containing NPCs-inspired system also responds to acidic microenvironment, as confirmed by electrochemical impedance spectroscopy (EIS) over a time range of 100 days (Fig. 4d). The impedance measured at the lowest frequency ($|Z|_{0.01Hz}$) reflects that the overall corrosion resistance of the hybrid coatings drops in early immersion time due to the penetration of corrosive solution and corrosion occurrence at coating/metal interface[45], but gradually increases towards the initial value in the following days, indicating a smart feedback to the microenvironmental pH lowering induced by minor corrosion. While there is only a steady impedance decrease for dummy coatings, implying a gradual defunction of free BTA. The visual observation of the coated samples from photographs taken after 100 days immersion is in good agreement with the EIS results (Figs. 4e-f). The pit-like defects and deposits of white corrosion products on the coating surface account for the deterioration of the dummy coating and corrosion attacks at coating/metal interface. In contrast, there are almost no coating cracks or delamination can be observed in the areas of the coating containing NPCs-inspired controlled release system, which indicates an appropriate fit of the pH sensitive nanovalves in prolonging the serving time of protective coatings.

## 4. Conclusions

Inspired by an effective biological valve system - nuclear pore complexes, which control the permeability with their 3D porous structure and reversible complexation with cargo molecules, we formed a novel nanovalve system with sensitivity to the external stimuli. We focused in this work mainly on investigating the selective permeability of nanovalves endowed by their reversible complexation with small functional cargo molecules and targeted at the encapsulation and controlled release of angstrom-sized species. Two theoretical models for explanation of nanovalve performance were proposed and confirmed by the experimental data obtained. The nanovalves exhibit effective control over inhibitor storage and release at different pH range. Finally, impregnation of these nanocontainers into commercial coatings provided them autonomous self-healing functionality for corrosion protection. The proposed nanovalves can be easily up-scaled to the substantial quantities for their implementation in other fields requiring storage and controlled release of small molecular species outside biomedicine and drug delivery.


## Acknowledgements

This work was financially supported by EU FP7 Byefouling project of EU Commission and Brian Mercer Feasibility Award of the Royal Society of Chemistry (UK).


## Notes and references


[a] Max-Planck Institute of Colloids and Interfaces, 14424, Potsdam, Germany.

[b] Stephenson Institute for Renewable Energy Department of Chemistry, University of Liverpool, Crown Street, Liverpool, L69 7ZD, UK.

[c] Fritz-Haber-Institut der MPG, Faradayweg 4-6, 14195, Berlin, Germany.

[d] International Center for Applied Mechanics, State Key Laboratory for Strength and Vibration of Mechanical Structures, Xi'an Jiaotong University, Xi'an, 710049, P.R.China


† Footnotes should appear here. These might include comments relevant to but not central to the matter under discussion, limited experimental and spectral data, and crystallographic data.

Electronic Supplementary Information (ESI) available: [details of any supplementary information available should be included here]. See DOI: 10.1039/b000000x/


1. B. M. Discher, Y. Y. Won, D. S. Ege, J. C. M. Lee, F. S. Bates, D. E. Discher and D. A. Hammer, *Science*, 1999, **284**, 1143-1146.
2. F. H. Meng, Z. Y. Zhong and J. Feijen, *Biomacromolecules*, 2009, **10**, 197-209.
3. H. B. Wang, F. M. Xu, D. D. Li, X. S. Liu, Q. Jin and J. Ji, *Polymer Chemistry*, 2013, **4**, 2004-2010.
4. A. Ribeiro, F. Veiga, D. Santos, J. J. Torres-Labandeira, A. Concheiro and C. Alvarez-Lorenzo, *J Membrane Sci*, 2011, **383**, 60-69.
5. A. Ribeiro, F. Veiga, D. Santos, J. J. Torres-Labandeira, A. Concheiro and C. Alvarez-Lorenzo, *Biomacromolecules*, 2011, **12**, 701-709.
6. J. Liu, W. Bu, L. Pan and J. Shi, *Angewandte Chemie International Edition*, 2013, **52**, 4375-4379.
7. N. A. Impellitteri, M. W. Toepke, S. K. L. Levengood and W. L. Murphy, *Biomaterials*, 2012, **33**, 3475-3484.
8. S. Jhunjhunwala, G. Raimondi, A. J. Glowacki, S. J. Hall, D. Maskarinec, S. H. Thorne, A. W. Thomson and S. R. Little, *Adv. Mater.*, 2012, **24**, 4735-4738.
9. W. A. Zhao, C. H. Cui, S. Bose, D. G. Guo, C. Shen, W. P. Wong, K. Halvorsen, O. C. Farokhzad, G. S. L. Teo, J. A. Phillips, D. M. Dorfman, R. Karnik and J. M. Karp, *P Natl Acad Sci USA*, 2012, **109**, 19626-19631.
10. K. Malachowski, J. Breger, H. R. Kwag, M. O. Wang, J. P. Fisher, F. M. Selaru and D. H. Gracias, *Angewandte Chemie International Edition*, 2014, **53**, 8045-8049.
11. V. Percec, A. E. Dulcey, V. S. K. Balagurusamy, Y. Miura, J. Smidrkal, M. Peterca, S. Nummelin, U. Edlund, S. D. Hudson, P. A. Heiney, D. A. Hu, S. N. Magonov and S. A. Vinogradov, *Nature*, 2004, **430**, 764-768.
12. V. Percec, A. E. Dulcey, M. Peterca, M. Ilies, S. Nummelin, M. J. Sienkowska and P. A. Heiney, *P Natl Acad Sci USA*, 2006, **103**, 2518-2523.
13. A. J. Kim, M. S. Kaucher, K. P. Davis, M. Peterca, M. R. Imam, N. A. Christian, D. H. Levine, F. S. Bates, V. Percec and D. A. Hammer, *Advanced Functional Materials*, 2009, **19**, 2930-2936.
14. X. Hou, H. C. Zhang and L. Jiang, *Angewandte Chemie-International Edition*, 2012, **51**, 5296-5307.
15. H. Zhang, X. Hou, L. Zeng, F. Yang, L. Li, D. Yan, Y. Tian and L. Jiang, *Journal of the American Chemical Society*, 2013, **135**, 16102–16110.
16. M. Manzano, M. Colilla and M. Vallet-Regi, *Expert Opin Drug Del*, 2009, **6**, 1383-1400.
17. D. Borisova, H. Mohwald and D. G. Shchukin, *Acs Nano*, 2011, **5**, 1939-1946.
18. J. J. Fu, T. Chen, M. D. Wang, N. W. Yang, S. N. Li, Y. Wang and X. D. Liu, *Acs Nano*, 2013, **7**, 11397-11408.
19. M. Szuwarzyński, L. Zaraska, G. D. Sulka and S. Zapotoczny, *Chemistry of Materials*, 2013, **25**, 514-520.
20. Y. Takemoto, H. Ajiro, T.-a. Asoh and M. Akashi, *Chemistry of Materials*, 2010, **22**, 2923-2929.
21. C. Wang, Z. X. Li, D. Cao, Y. L. Zhao, J. W. Gaines, O. A. Bozdemir, M. W. Ambrogio, M. Frasconi, Y. Y. Botros, J. I. Zink and J. F. Stoddart, *Angewandte Chemie-International Edition*, 2012, **51**, 5460-5465.
22. B. Burke, *Science*, 2006, **314**, 766-767.
23. M. Elbaum, *Science*, 2006, **314**, 766-767.
24. D. Gorlich and U. Kutay, *Annu Rev Cell Dev Bi*, 1999, **15**, 607-660.
25. S. Frey, R. P. Richter and D. Goerlich, *Science*, 2006, **314**, 815-817.
26. S. Frey and D. Gorlich, *Cell*, 2007, **130**, 512-523.
27. S. Angelos, N. M. Khashab, Y. W. Yang, A. Trabolsi, H. A. Khatib, J. F. Stoddart and J. I. Zink, *Journal of the American Chemical Society*, 2009, **131**, 12912-12913.

28. M. J. Hollamby, D. Fix, I. Donch, D. Borisova, H. Mohwald and D. Shchukin, *Adv. Mater.*, 2011, **23**, 1361-1365.
29. J. D. Donaldson and D. Beyersmann, in *Ullmann's Encyclopedia of Industrial Chemistry*, Wiley-VCH Verlag GmbH & Co. KGaA, Editon edn., 2000.
30. M. Ocak, N. Gümrükçüoğlu, Ü. Ocak, H.-J. Buschmann and E. Schollmeyer, *J Solution Chem*, 2008, **37**, 1489-1497.
31. D. Tarn, M. Xue and J. I. Zink, *Inorganic Chemistry*, 2013, **52**, 2044-2049.
32. Y. Li, M. L. Gong, K. Ramji and Y. Z. Li, *Journal of Physical Chemistry C*, 2009, **113**, 18003-18013.
33. R. Xu and H. C. Zeng, *The Journal of Physical Chemistry B*, 2003, **107**, 12643-12649.
34. Z. Zheng, X. Huang and D. Shchukin, *Chemical Communications*, 2014, **50**, 13936-13939.
35. S. Chaberek, R. C. Courtney and A. E. Martell, *Journal of the American Chemical Society*, 1952, **74**, 5057-5060.
36. J. W. Bunting and K. M. Thong, *Canadian Journal of Chemistry*, 1970, **48**, 1654-1656.
37. D. W. Schaefer, A. J. Hurd, D. K. Christen, S. Spooner and J. S. Lin, *MRS Online Proceedings Library*, 1988, **121**, 305-312.
38. D. W. Schaefer and K. D. Keefer, *Phys Rev Lett*, 1986, **56**, 2199-2202.
39. C. J. Brinker, K. D. Keefer, D. W. Schaefer and C. S. Ashley, *J Non-Cryst Solids*, 1982, **48**, 47-64.
40. D. W. Schaefer and K. D. Keefer, *Phys Rev Lett*, 1984, **53**, 1383-1386.
41. G. E. Amidon, W. I. Higuchi and N. F. H. Ho, *J Pharm Sci*, 1982, **71**, 77-84.
42. B. H. Loo, A. Ibrahim and M. T. Emerson, *Chemical Physics Letters*, 1998, **287**, 449-454.
43. P. DeMuth, M. Hurley, C. W. Wu, S. Galanie, M. R. Zachariah and P. DeShong, *Microporous and Mesoporous Materials*, 2011, **141**, 128-134.
44. J. R. Davis, *Corrosion: Understanding the Basics*, A S M International, 2000.
45. D. Borisova, D. Akçakayıran, M. Schenderlein, H. Möhwald and D. G. Shchukin, *Advanced Functional Materials*, 2013, **23**, 3799-3812.
46. D. Fix, E. V. Skorb, D. G. Shchukin and H. Mohwald, *Meas Sci Technol*, 2011, **22**.
47. D. Borisova, H. Mohwald and D. G. Shchukin, *ACS Applied Materials & Interfaces*, 2012, **4**, 2931-2939.